RESEARCH PAPER

Centrifuge modelling of rainfall-induced slope failure in variably saturated soil

Shun Wang[1] · Gregor Idinger[1] · Wei Wu[1]

Abstract

This paper presents the results of centrifuge tests on rainfall-induced instabilities in variably saturated slopes. The roles of rainfall intensity and initial conditions, such as slope angle, porosity and degree of saturation of the soil, in the failure initiation and postfailure kinematics are considered. The failure patterns, infiltration profile and deformation at prefailure and postfailure stages are characterized. The results indicate that rainfall-induced slope failures usually follow one of the following two failure modes, i.e. slide-to-flow and flowslide failure modes. The former pattern is characterized by soil mass flow after initial failure along a continuous shear surface, while the latter is more relevant to the rapid increase in the saturation at the slope surface, resulting in surface erosion channels followed by the acceleration of the soil mass. The flowslide failure pattern usually gives rise to several superficial shear surfaces and longer run-out distances. The rainfall intensity and profiles of the degree of saturation play the key roles in initiating the slope failure at the prefailure stage and subsequently in mobilizing the soil mass at the postfailure stage. Our test data, together with the data from the literature, are presented in two threshold curves to define the critical condition of slope failure under rainfall infiltration.

Keywords Centrifuge test · Flowslide · Partially saturated soil · Slope stability · Threshold curve

1 Introduction

Rainfall-induced landslides in partially saturated soil deposits constitute one of the most recurrent and destructive natural hazards around the world [18, 24]. Many authors claim that the quick loss of matric suction due to rainfall infiltration, and the subsequent development of positive pore pressures due to the formation of a perched water table as the most important triggering factors for such landslides [20, 26, 40]. The increase in pore pressure may instantly decrease the effective stress in the soil, thereby reducing the safety factor of a slope and triggering a landslide with an initial acceleration [18, 19]. The rapid movement of the sliding masses with rainwater may lead to the transition of the mechanical response of the soil from frictional type to a viscous type and thus produce flow-type landslides [39]. Those landslides typically travel long

distances at high velocities with large mobilized volumes and thus difficult to prevent under natural conditions [12], causing a large number of casualties and economical losses annually.

The failure patterns of rainfall-induced slopes instability are commonly recognized as "slide" at the prefailure stage and "slide-to-flow" or "flowslide" at the postfailure stage [4, 5]. Various mechanisms have been invoked to explain the failure mechanism of different types: a slide occurs when limit equilibrium state is gradually reached on a potential shear surface so that the balance between driving and resisting forces is broken. This may due to the progressive loss of matric suction in variably saturated slopes upon infiltration of rainfall. The transition from a slide to a flow is mostly caused by the development of totally or partially undrained conditions during heavy rainfall events. This may arise cascading effects of local failure and variation in slope geometry, leading to an abrupt change of the stress state, and thus resulting in slide turning into flows, sometimes before full saturation is reached. While the previous two categories are independent on the soil constitutive behaviour, flowslides are related to static

✉ Wei Wu
  wei.wu@boku.ac.at

1 Institut für Geotechnik, Universität für Bodenkultur Wien, Feistmantelstrasse 4, 1180 Vienna, Austria

liquefaction [41, 43] or soil mechanical instability phenomena [8]. This type of failure is characterized by fast and furious flows of soil masses. The kinematics of the flowslides are largely dictated by the viscous behaviour of the saturated soil–water mixture.

Open questions may derive from the variability of the failure mechanisms, often implying the coexistence of slides of limited mobility and rapid flowslides across the same site. Such different mechanisms are caused by specific combinations of rainfall scenarios and slope conditions, such as slope angle, porosity and degree of saturation [33–35], and call for accurate characterization of their initiation and postfailure processes. However, current hypotheses as to the physical processes behind how precipitation initiates slope instabilities and subsequently dominates postfailure patterns are based mostly on in situ observations [15, 32, 38] and full-scale tests [17, 27], which are generally costly and irreproducible. Although some efforts based on centrifuge model tests provide a basis to quantify the susceptibility to failure [16, 22, 46, 49], none of them linked the initial slope conditions to the failure patterns of slopes under variable rainfall scenarios. Thus, we still lack well-instrumented and documented physical models to confirm the mechanisms involved. On the other hand, rainfall infiltration in unsaturated soil deposits has been the object of several theoretical and numerical studies [1, 6, 24, 36]. Those models rely on comprehensive experimental data obtained from element tests and physical model tests. However, there is a serious lack of a database of model tests at the prototype scale for the development and validation of such numerical models.

In this study, we aimed to characterize the initiation processes and postfailure patterns of rainfall-induced slope instabilities. The complex hydro-mechanically coupled behaviour is modelled with simplified slope geometry and boundary conditions through centrifuge modelling. This study highlights the importance of rainfall scenarios, e.g. moderate, heavy and torrential rainfall events, together with the roles of unsaturation, porosity and slope geometry, in the failure initiation and postfailure kinematics of homogenous soil slopes. These experiments are well controlled and allow us to quantify the critical conditions leading to failure of partially saturated slopes under the effect of rainfall infiltration.

2 Centrifuge modelling

The main principle of centrifuge modelling is to simulate the stress state in a prototype under an induced acceleration field [23]. As the acceleration increases to n times that of Earth's gravity, the dimensions of the model are scaled by n times [44]. Centrifuge modelling tests allow simulating hazardous landslides on models of reduced size. The model slope can be fabricated repeatedly under well-defined boundary conditions. The repeatability of centrifuge model tests greatly simplifies the analysis of individual parameters governing the instability process. Thus, this technique permits the exploration of slope stability problems representative of field-scale behaviour.

2.1 Model set-up and rainfall device

The centrifuge facility at our laboratory has a nominal radius of 1.31 m and a maximum centrifugal acceleration 200-g. A strongbox shown in Fig. 1a is used to accommodate the model slope. The strongbox, with an inner dimension of $480 \times 155 \times 450$ mm (length × width × height), is mainly made of aluminium alloy. The top plate of the strong box has a recess hole for the sensors and water supply hoses for rainfall simulation. The base plate is rigidly connected to the swinging platform. A transparent front wall of acrylic is used as an observation window to view the side profile of the model slope. A digital camera is equipped in front of the observation window to track the soil displacement. In addition, a high-speed video camera is placed inside the strongbox to record the deformations of the slope surface.

To construct the model slope, a soil cuboid with a dimension of $480 \times 155 \times 250$ mm is firstly made by compacting 10 soil layers, each with equal thickness. The slope is then cut from the compacted soil cuboid. In doing so, the front and back walls of the strongbox are temporarily replaced by wooden templates. Two pairs of wooden templates with slope angles of 35° and 45° are used to aid the slope construction. Following the geometries of the wooden templates, it is easy to cut a model slope from the soil block. Finally, the wooden template are replaced with the walls of the strong box. The model slope was covered with a plastic sheet and cured overnight before rainfall tests for gaining a uniform distribution of moisture in the soil. Details on the dimension of the slopes are shown in Fig. 1b, c. The friction between the soil and the rear and the acrylic front wall should be minimized to maintain undisturbed plane strain conditions. For this purpose, a thin film of transparent silicon oil is applied on the inner surface of the front and rear wall before each test. This lubricant reduces wall friction and minimizes its effect on the soil deformation.

On the other hand, a new device is developed for simulating rainfall in the centrifuge facility. The rainfall system consists of a water tank for rainwater storage, a water line connecting the tank to the model box and a distribution system with perforated hoses located in close vicinity above the slope surface. Figure 2a shows the main
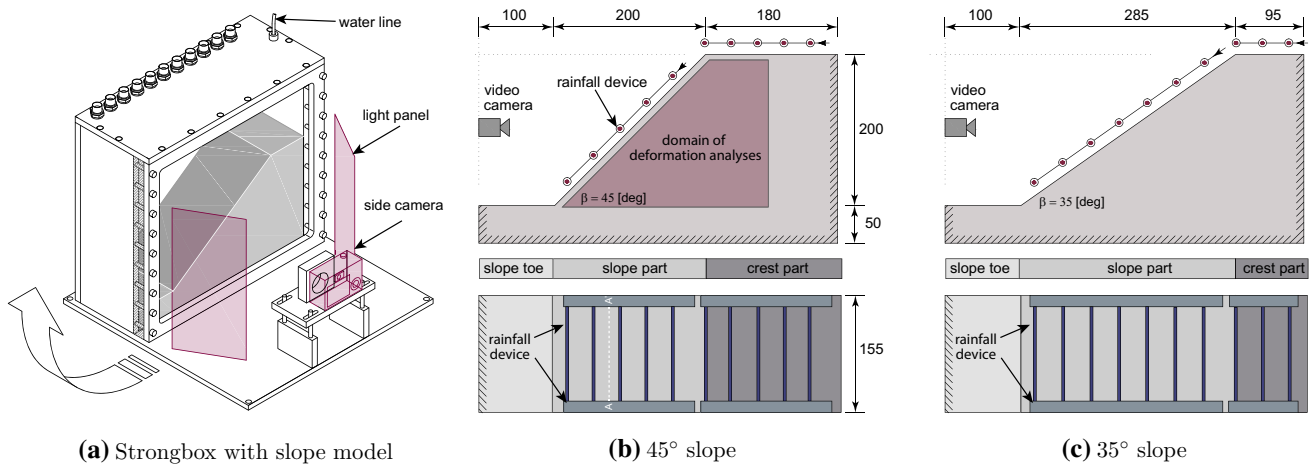
(a) Strongbox with slope model   (b) 45° slope   (c) 35° slope

Fig. 1 Dimension and set-up of the centrifuge model: **a** centrifuge strongbox with a model slope, **b** side view of 45° and **c** 35° slopes with the rainfall system (unit: mm)
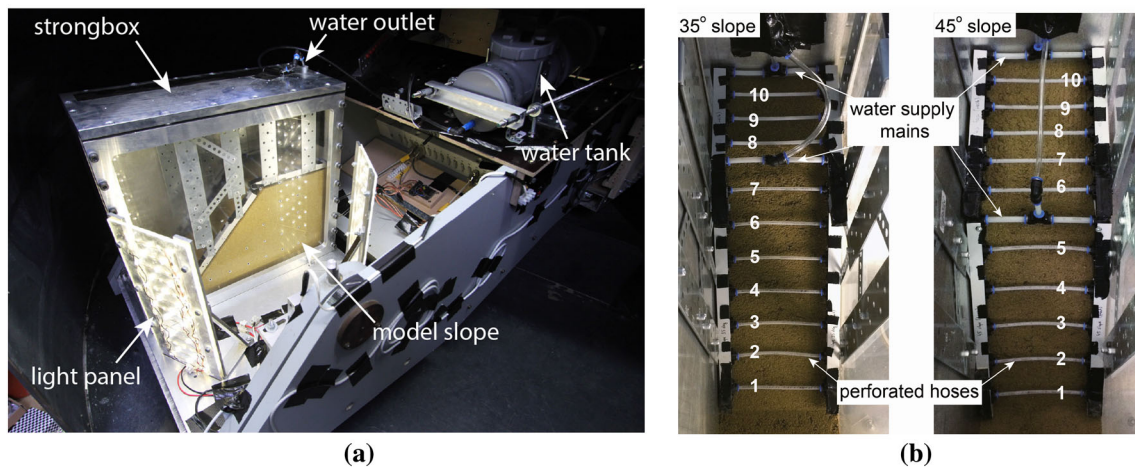

Fig. 2 Centrifuge model with the rainfall system: **a** components of the rainfall device and **b** distribution of the perforated hoses for 35° and 45° slopes

components of the rainfall system. The rainfall system adopts the principle of drip irrigation usually used in agriculture. An array of perforated hoses are placed close above the slope surface to discharge the rainwater. As shown in Fig. 2b, the perforated hoses are aligned parallel to the slope toe line. The horizontal spacing between the two adjacent hoses is 35 mm. To follow the geometry of the slope, two sets of perforated hoses are used: one for the crest and the other one for the inclined slope section. This configuration leads to different number of perforated hoses at the crest and the slope section. For instance, for a 35° slope, 7 perforated hoses are placed above the slope section and the rest 3 ones are fixed at the crest, while for a 45° slope, the same number of perforated hoses are distributed at the crest and the slope section (see Figs. 1b, c and 2b). The rainfall intensity depends on the centrifuge acceleration and the flow rate of the water supply, which is controlled by the size and number of the tiny pinholes in the

hose walls. A wide range of rainfall intensities from 2.5 to 30 mm/h can be simulated by this device. With the largest rainfall intensity, i.e. 30.0 mm/h, the diameter of the raindrops may reach up to 500 μm with an ultimate velocity of approximately 0.7 m/s at 30-g level, resulting in an impact force of approximately 10 pa at the slope surface. This observation suggests that the raindrops delivered by the larger pinhole may cause a certain erosion at the slope surface. To minimize this effect, all the centrifuge tests, except the test CRF-08 (see Table 1), adopt rainfall intensities that are smaller than 15.0 mm/h. On the other hand, this device is able to generate a uniform rainfall overall on the slope surface, while it may give rise to localized infiltration below the perforated hose due to its drip delivery nature. Details for the calibration of the rainfall device can be referred to our companion paper [47].

Table 1 Experimental programme and results of the centrifuge tests

Test ID	Initial slope conditions				Rainfall			Failure		
	g-level [g]	β_0 [deg]	e_0 [−]	w_0 [%]	I_P [mm/h]	D_M [s]	R_M [ml]	$t_{f,M}$ [s]	$t_{f,P}$ [h:min]	Type A/B
CRF-01	30	45	0.91	6.0	14.8	106	728	19	04:47	A
CRF-02	30	45	0.91	6.0	15.9	180	1059	13	03:17	A
CRF-03	30	45	0.91	11.5	11.8	96	523	40	10:04	A
CRF-04	30	45	0.91	11.6	10.5	103	498	14	03:32	A
CRF-05	30	45	0.76	11.3	10.1	150	702	60	15:06	A
CRF-06	30	45	0.75	11.3	10.0	210	967	154	38:47	A
CRF-07	30	45	0.73	14.7	11.6	130	699	26	06:32	B
CRF-08	30	45	0.72	11.3	27.0	60	749	4	01:00	B
CRF-09	30	45	0.73	15.0	5.8	320	859	94	23:48	A
CRF-10	30	45	0.74	11.5	4.9	410	924	–	–	–
CRF-11	30	35	0.91	6.3	13.2	140	852	36	09:04	B
CRF-12	30	35	0.90	11.5	12.0	220	1224	–	–	–
CRF-13	30	35	0.74	11.5	12.6	325	1897	256	64:09	A
CRF-14	30	35	0.75	15.1	12.9	110	655	40	10:19	B
CRF-15	30	35	0.78	11.5	13.5	230	1433	51	12:50	B
CRF-16	30	45	0.91	11.5	13.6	100	628	12	03:01	A
CRF-17	30	45	0.74	11.6	12.4	210	1214	49	12:28	A
CRF-18	30	45	0.74	11.5	12.4	180	1034	22	05:33	A

β_0: slope angle, e_0: initial void ratio, w_0 initial water content, I: rainfall intensity, D: rainfall duration, and R: accumulated rainfall, t_f initial failure time. The subscripts M and P denote model and prototype scale, respectively. - denotes no failure; Type A and B denote 'slide-to-flow' and 'flowslide', respectively.

2.2 Slope soil

The soil used to construct the model slope is classified as well-graded silty sand. Figure 3 shows the grain size distribution of the soil. The particle sizes range from 0.002 mm to 4.0 mm, with a mean grain diameter d_{50} of 0.23 mm. The particle density of the soil is $\rho_s = 2.67\,\text{g/cm}^3$. The maximum and minimum void ratios of the soil are $e_{\min} = 0.45$ and $e_{\max} = 1.09$, respectively. The sub-angular shape of the granular particles can be visualized from the
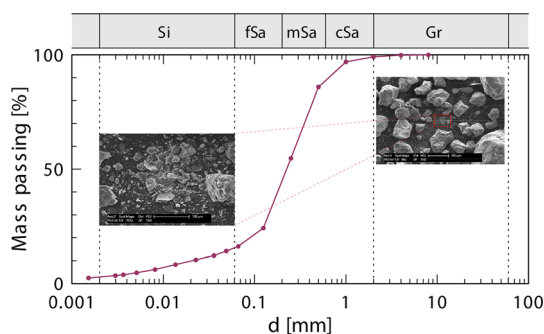

Fig. 3 Grain size distribution curve of the silty sand with SEM image of the granular particles (Si—silt, fSa—fine sand, mSa—medium sand, cSa—course sand and Gr—gravel)

scanning electron microscope (SEM) images. A fraction of silt and clay is also observed in the soil sample.

The soil–water retention curves (SWRC) are obtained based on the Fredlund and Xing model [9], in which the degree of saturation S_r is expressed as:

$$S_r = \frac{C(\psi, \psi_r)}{\left[\ln\left[e + (\psi/a)^n\right]\right]^m} \tag{1}$$

where n and m are empirical parameters and a is related to the air entry value. The numerator is a correction function depending on the matric suction ψ and ψ_r (the suction at the residual water content w_r). e is the Euler's number, which should be differentiated from the void ratio. Figure 4a shows the drying branch of the SWRC of the silty sand with different densities by using the fitting parameters a, n and m. The cross marks denote the experimental data for the triaxial compression tests with $\psi = 10\,\text{kPa}$.

The hydraulic conductivity curves are obtained based on the Mualem–van Genuchten formulation [29]:

$$k = k_{\text{sat}} \sqrt{S_e}\left[1 - \left(1 - S_e^{1/m}\right)^m\right]^2 \tag{2}$$

where k_{sat} is the saturated hydraulic conductivity and $S_e = [(w - w_r)/(w_{sat} - w_r)]$ is the effective saturated saturation. Figure 4b shows the hydraulic conductivity curves for

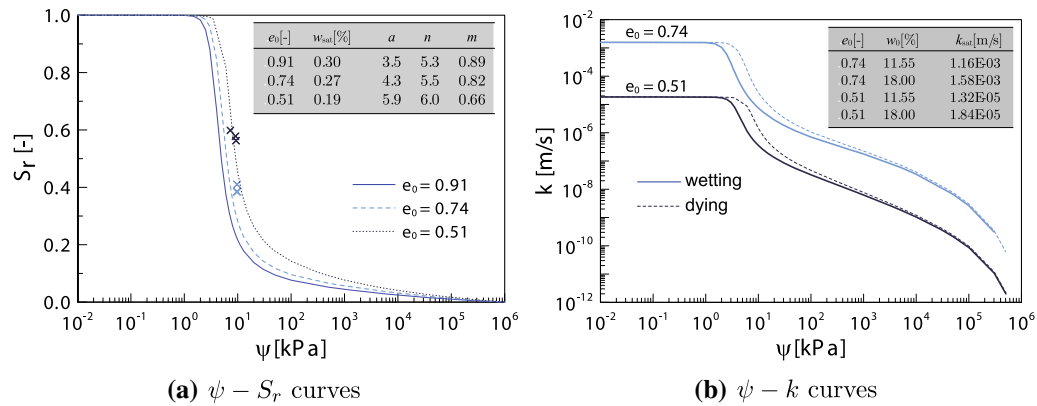**(a)** $\psi - S_r$ curves　　　　　　　　　**(b)** $\psi - k$ curves

Fig. 4 Hydraulic properties of the of the silty sand: **a** drying branch of soil–water retention curves based on the Fredlund and Xing model [9] and **b** hydraulic conductivity curves based on the Mualem–van Genuchten formulation [29]

drying and wetting together with k_{sat} at different water contents for dense and medium dense soils. It can be seen that the hydraulic conductivity decreases with the matric suction. At the same matric suction, the derived hydraulic conductivity in the drying path is larger than that in the wetting path.

Generally, unsaturation can influence the mechanical behaviours of the soil. In this paper, the shear strength of the unsaturated soil is determined by the extended Mohr–Coulomb criterion with:

$$\tau = c' + (\sigma - u_a)\tan\phi' + (u_a - u_w)\tan\phi^b \quad (3)$$

where σ, u_a and u_w are the total stress, pore air pressure and pore water pressure, respectively, and $(u_a - u_w)\tan\phi^b$ can be regarded as the apparent cohesion of the unsaturated soil with $(u_a - u_w)$ denoting the matric suction.

The mechanical behaviours of the soil at saturated and partially saturated states are determined by a double-cell triaxial apparatus in our laboratory. Four sets of triaxial compression tests on the soil with medium dense $e_0 = 0.74$ and very dense $e_0 = 0.51$ compaction state under both saturated and unsaturated conditions are carried out. The matric suction in the unsaturated state is $\psi = 10$ kPa. This value corresponds to the intersection of the transition and residual zone of the soil–water retention curve. Each set of test involves three different effective confining pressures, namely $\sigma'_3 = 50, 100, 200$ kPa. The triaxial compression is conducted by applying an axial strain rate of 0.01 %/min. This strain rate guarantees a drained condition during the test. Figure 5 shows the stress–strain and volumetric behaviours of the soil at different states. It can be seen that the soil shows strain hardening and volumetric contraction behaviours at medium dense state, while a pronounced strain softening and dilatancy is observed at a very dense state. In accordance with Eq. (3), the peak shear strength of the soil under saturated condition is $\phi'_p = 31.8°$ and $c'_p = 0.0$ kPa for the medium dense state and $\phi'_p = 38.1°$ and

$c'_p = 15.0$ kPa for the very dense state. The matric suction gives no influence on the peak friction angle, but leads to an increase in the cohesion by approximately 6 kPa and 20 kPa for the medium dense and very dense states, respectively. This result shows that the silty sand is a non-cohesive soil in regard to the medium dense state, but exhibits considerable apparent cohesion in very dense and partially saturated states.

2.3 Test programme and results

In total, 18 centrifuge tests with different initial conditions and rainfall intensities are conducted. The initial slope conditions include slope angle β_0, void ratio e_0 and water content w_0. Most of the slopes are inclined at 45°, with only five 35° slopes for comparison. The slopes are compacted at two densities, namely, a loose compaction state with $e_0 = 0.91$ and a medium dense state with $e_0 = 0.74$. For each compaction state, two different initial water contents are adopted, i.e. $w_0 = 6.0\%$ ($S_r = 0.20$) and 11.5% ($S_r = 0.40$) for loose state, and $w_0 = 11.5\%$ ($S_r = 0.35$) and 15.1% ($S_r = 0.55$) for medium dense state. Thus, four initial soil conditions are included in the test programme. All the model tests are performed at 30-g level, at which the slope remains initially stable under the enhanced gravity loads. This g-level implies that a model slope of 250 mm height represents a prototype slope of 7.5 m height.

These slopes are exposed to three types of rainfall intensities, i.e. $I_P = 5$, 12 and 27 mm/h, representing moderate, heavy and torrential rainfall events, respectively, at the prototype scale. The rainfall is initiated after the geostatic equilibrium is achieved at the prescribed gravity. The rainfall is persisted for a while after the initial failure. This allows us to observe the subsequent propagation stages of progressive failure. The rainfall duration and accumulated rainfall as well as the slope failure time are
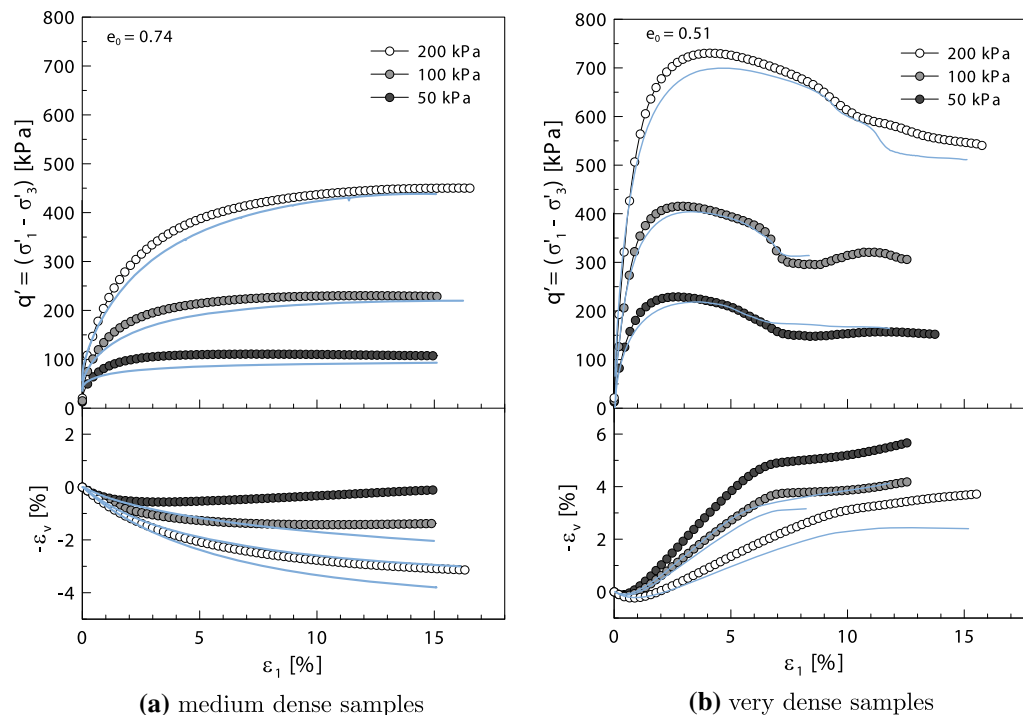
Fig. 5 Stress–strain and volumetric behaviours of medium and very dense samples at saturated and partially saturated (matric suction $\psi = 10$ kPa) states in drained triaxial compression tests (solid line for saturated condition and line with symbol for unsaturated condition)

acquired in each test. In addition, the failure pattern of each slope is determined whether slope failure occurred. This regard will be interpreted in detail in the next section. Details on the experimental programme and the results are presented in Table 1. It can be seen that the initial soil conditions and rainfall intensities for all tests violate slightly from the prescribed values. This result, attributed to the error during slope construction, is very common in physical modelling.

3 Experimental observations

During the tests, the failure processes of all slopes are observed through the side camera and the front high-speed video camera. Generally, the progressive failure process is consisted of a prefailure stage after initial settlement and a postfailure stage with large deformation. In the following, the experimental observations, such as slope failure patterns, infiltration profile and deformations at prefailure and postfailure stages, are characterized.

3.1 Failure patterns

It is observed that, except the slopes CRF-10 and CRF-12, all the slopes exhibit flow-type failure under the effect of rainfall infiltration. According to the failure mechanisms outlined by Cascini et al. [4, 5], the postfailure patterns can

be categorized into slide-to-flow and flowslide. Two slopes, namely CRF-16 and CRF-07, are selected to show the basic feature of the failure patterns. Both slopes are inclined at 45° and exposed to heavy rainfall of approximately 12 mm/h, while they possess different initial soil conditions.

The slide-to-flow failure pattern is represented by the CRF-16 slope shown in Fig. 6a. The onset of failure is characterized by the appearance of tension cracks at the surface ($t = 18$ s), resulting in a local slip at the toe of the slope ($t = 23$ s). The local slip extends from the toe to the crest of the slope and leads evidentially to a global slide of the slope ($t = 25$ s). After the deposition of the primary sliding mass ($t = 27$ s), fast flows of soil mass with various volume run off continuously from the top of the slope, eroding the slope surface and the deposited soil mass ($t = 28 - 53$ s).

On the other hand, the flowslide failure pattern is represented by the CRF-07 slope. As shown in Fig. 6b, the failure is initiated by local surface erosion ($t = 5$ s). Local erosion channels are created by the stepwise enlarging through small discrete failures until a larger soil mass from upslope is destabilized, which commonly fails as rapid flows ($t = 24$ s). It is believed that local undrained condition could occur during this process. The highly saturated soil mass mobilizes downslope and causes several erosion channels, which forms a direct connection between the upper and the downslope. Finally, the progressive erosion of the channels triggers very rapid flows from the top
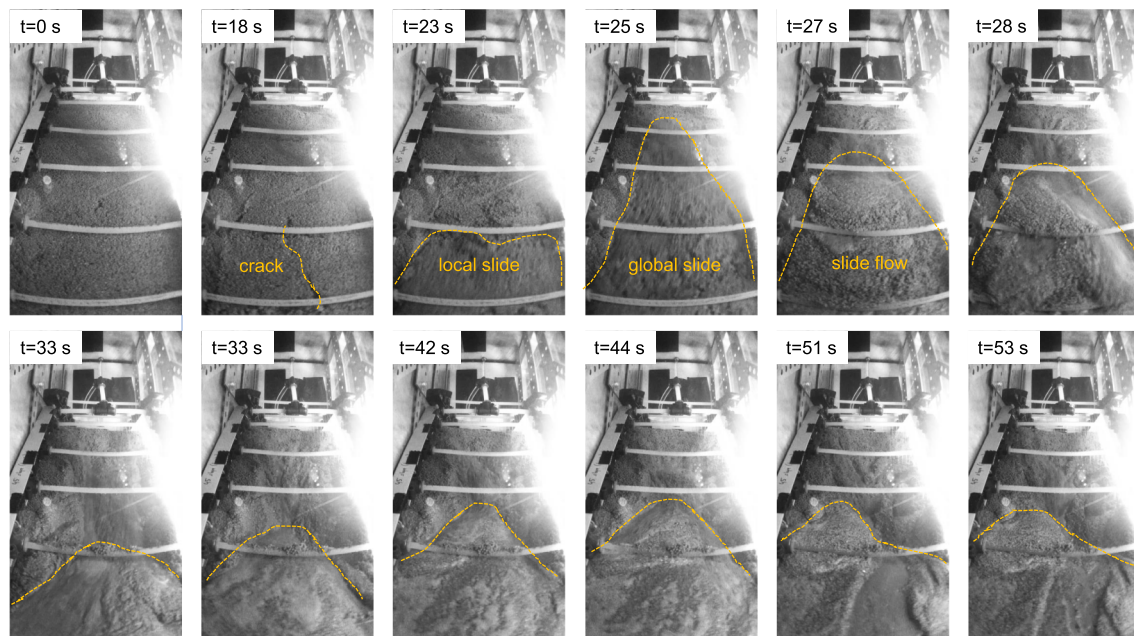
(a) Type A *Slide-to-flow*: CRF-16 with $e = 0.91$, $S_{r,0} = 0.35$, and $I_P = 13.6$ mm/h
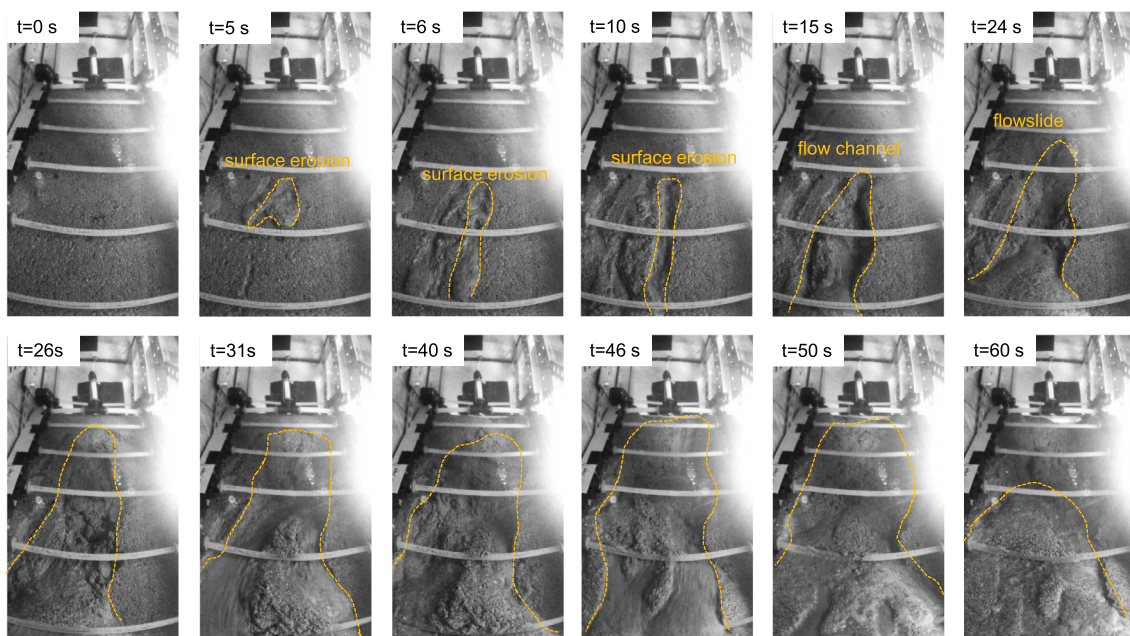
(b) Type B flowslide: CRF-07 with $e = 0.74$, $S_{r,0} = 0.55$, and $I_P = 11.6$ mm/h

Fig. 6 Time series views of the slope failure under the effect of rainfall infiltration

region. After a short period without failure deformations, the second phase of flowslide failures occurs. This failure mechanism is very similar to the backward erosion piping due to the sudden application of critical and supercritical hydraulic loads [45].

Figure 7 presents the failure process of all slopes in terms of failure initiation, slide regime and flow regime. The time that differentiates the failure regimes is obtained by analysing the images taken by the high-speed camera. The initial failure is determined at the appearance of tension cracks, soil erosion by surface run-off and creep deformation. It is found that, for 35° slopes, 3 out of 4 slopes failed as flowslide, only the slope CRF-13 with medium dense compaction and low antecedent rainfall is classified as slide-to-flow failure. For 45° slopes, only two slopes, namely CRF-07 with high antecedent rainfall and
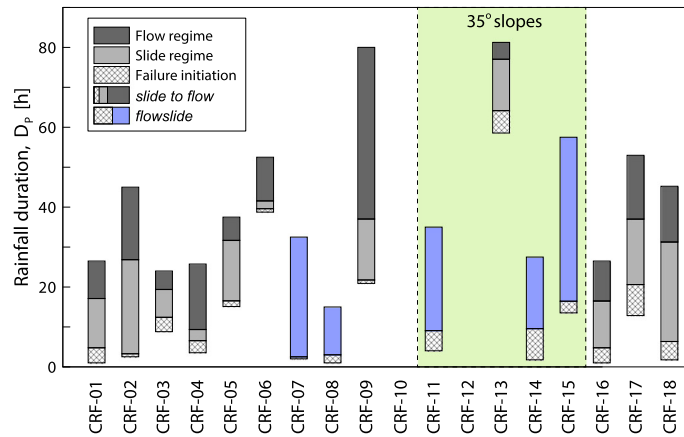
Fig. 7 Failure initiation and failure regimes over rainfall duration

CRF-08 exposed to torrential rainfall, fail as flowslide type. Generally, tests with similar slope conditions and rainfall intensities may fail following the same failure pattern but slightly different critical rainfall durations. Moreover, the 45° slopes usually yield a shorter failure initiation than those of the 35° slopes.

3.2 Infiltration profile

The wide range of the critical rainfall durations which trigger slope failure allows us to plot the infiltration profile over time for slopes with similar initial conditions. The infiltration profile is represented by the water content of the soil below the slope crest after the tests. To account for the slight variations in rainfall intensities, the normalized rainfall duration t^* is adopted, i.e. $t^* = R_M/\bar{I}_M$ with $\bar{I}_M = 5.75$ mm/s being the average rainfall intensity for heavy rainfall event at model scale.

As presented in Fig. 8, each line represents the post-failure hydraulic state of a different centrifuge test,

including most of the slopes exposed to heavy rainfall events. The infiltration pattern is similar for all four initial soil conditions. The wetting front infiltrates under a certain gradient into deeper regions of the slope. The rainwater infiltrates faster for the slopes with loose densities and/or higher initial degree of saturation. It is observed that the water content of the soil increases to a threshold of about 16%; then, the subsequent rainwater flows primarily downwards owing to the high hydraulic conductivity of the slope (e.g. CRF-01, CRF-03 and CRF-04, also see Fig. 4b). This threshold value of the wetting front seems independent on the initial saturation nor the soil porosity. With increasing the rainfall duration, the rainwater may infiltrate until the impermeable base, saturating the soil at the bottom of the slope. Then the degree of saturation begins to increase from the bottom to the slope surface, resulting in reversed gradients of the infiltration profile (e.g. CRF-12, CRF-13 and CRF-17).
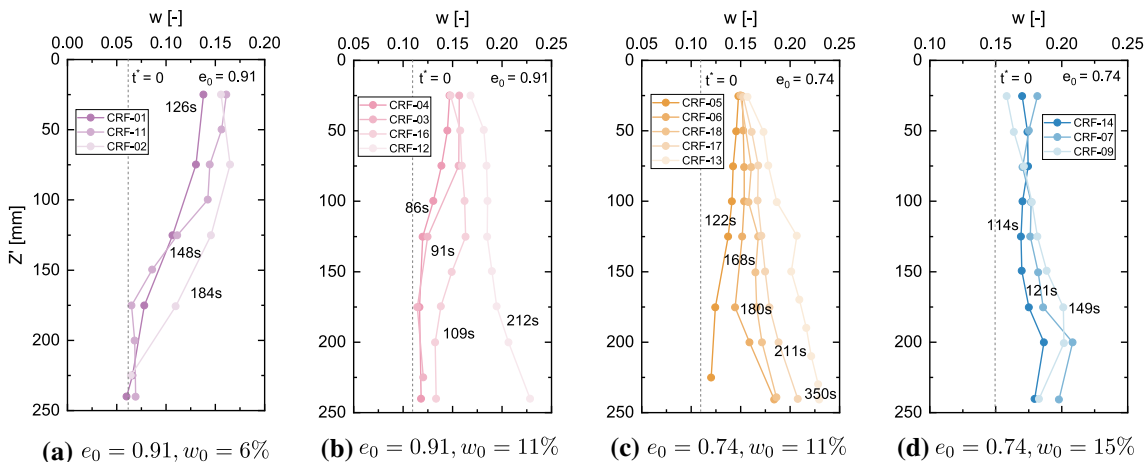

Fig. 8 Rainfall infiltration profiles over the normalized time t^*, based on the postfailure water content measurements in the crest region of slopes

3.3 Prefailure deformation

Prefailure movements include all the movements that occur before the failure initiation [18, 19]. They are resulted from creep, compaction due to wetting and self-weight and displacements associated with progressive failure. The prefailure process can be observed from the observation window of the strongbox with the help of the particle image velocimetry (PIV) image analysis code GeoPIV [48]. Images of the slope profile were taken through the transparent side wall of the strongbox using the side digital camera.

Figure 1b shows the domain of deformation, from where the kinematics of the slope at prefailure stage can be analysed. Figure 9a presents the accumulated deformation of a representative slope, e.g. CRF-03 slope. Both horizontal and vertical deformations initiate first and propagate from the upper half of the slope. With continuing rainfall, the magnitudes of the downward displacement increase, whereas the highest deformation is located at the crest region of the slope. The evolution of the shear zone is visualized in Fig. 9b. After 20 s rainfall, a discontinuous shear zone appears at the mid-height of the slope. The shear zone becomes evident and extends to both the crest

and lower parts. With continuous rainfall, a complete shear surface is eventually generated.

It is observed that the application of rainfall brings the slope to failure in 40 s, with the shear surface developed mainly in the superficial part of the slope. This may be attributed to the wetting compaction within the infiltration zone of the top soil, because the matric suction decreases as the wetting front descends. In addition, the cohesive and frictional components of the soil strength increase with depth, and thus, it is impossible to develop a deep-seated shear surface in the slope. Moreover, the prefailure process of the slope indicates a translational failure model, whereas the slope failure caused by increasing g-level without rainfall renders normally a pull-type failure with the maximum prefailure deformation occurred at the toe of the slope [14].

3.4 Postfailure displacement

The postfailure stage starts from the failure initiation until the mass of soil involved essentially stops moving [18]. The postfailure movements can be illustrated by the time–space graphs, taken from the high-speed video placed in front of the slope. The space–time plots allow studying the deformation of the slope throughout a longer period of

(a) Cumulated prefailure displacement
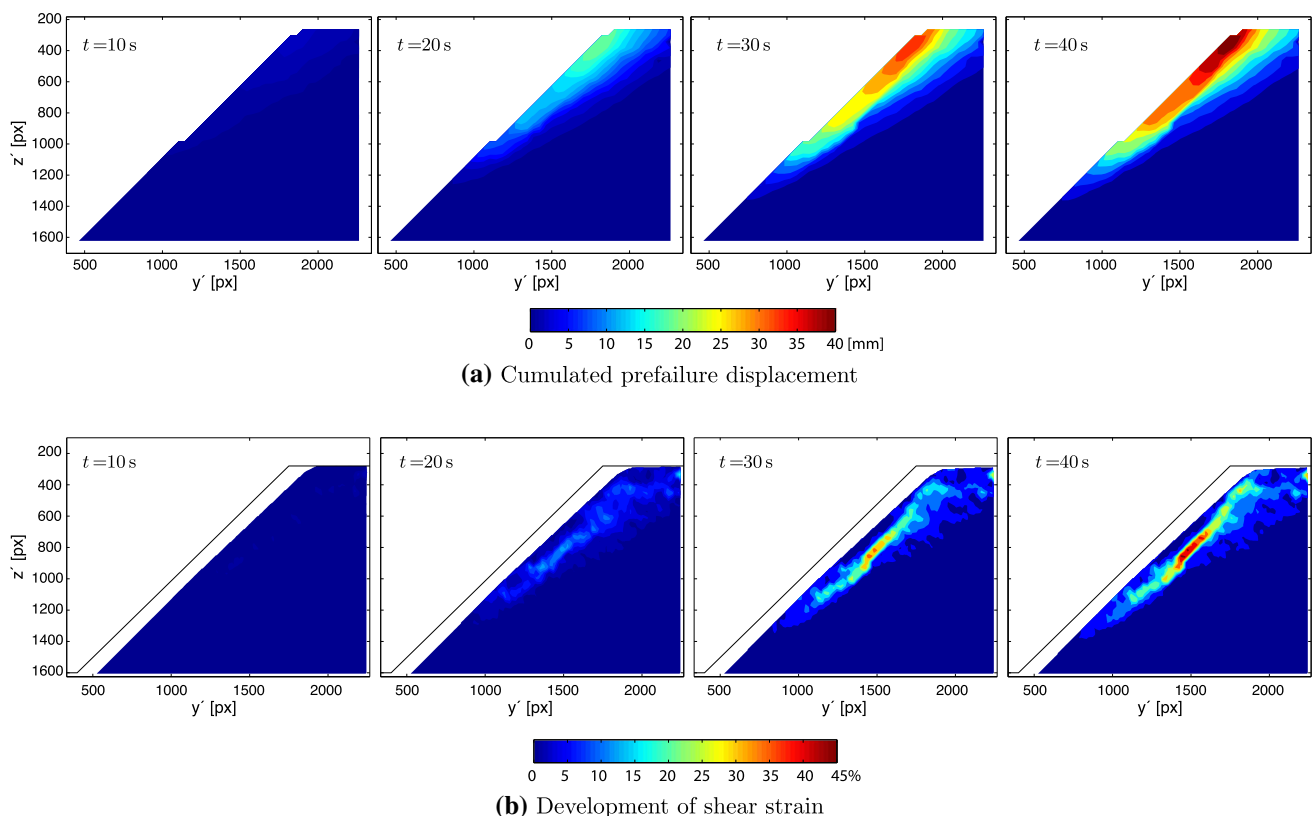

(b) Development of shear strain

Fig. 9 Progressive failure in the prefailure stage of slope CRF-03 under the effect of rainfall infiltration

time. The soil deformation is represented by a reference line of the width of 1 pixel, which is extracted from the video image and plotted over time. In our test, a horizontal profile close to the toe of the slope is selected as the reference line, as outlined by section A–A′ in Fig. 1b. More details refer to time–space plot can be found in the literature [2].

Figure 10 shows the space–time graphs of both failure types for selected slopes. The x-axis denotes the rainfall duration, while the y-axis presents the image of the slope surface along with A–A' section. As shown in Fig. 10a, the slopes following slide-to-flow failure pattern show relatively uniform deformations along the width of the slope. The initial failure is usually followed by a postfailure regime in the form of sliding and flowing. Figure 10b shows some typical time–space graphs of flowslide failure type. Clearly, the slope failure is initiated by local soil erosion, resulting in flow channels on the slope surface. With a clear front and convergent tail, the mass flows move rapidly along the channels to the toe of the slope. It is observed that the flow channels may develop separately or merge into a bigger one. Let us take the CRF-08 slope with the torrential rainfall event for example. It is observed that several surface channels merge to two main flow channels, which located on both sides of the slope. Although the space–time plots show different failure in morphology, some general features in their kinematics can be concluded.

Figure 11 shows the displacement paths and velocities at the slope surface during the whole failure process of slopes CRF-16 and CRF-07. The initial positions of the marker points are illustrated in the embedded picture. The top part of the figures presents displacement paths of marker point, while the bottom part shows the derived velocity of those tracked marker points. The initial positions of the marker points are illustrated in the embedded picture. For the slide-to-flow failure mode, the displacement paths of the tracked points increase in an exponential manner prior to the primary sliding failure. The soil closer to the crest of the slope yields the largest deformation during the primary slide. The peak velocities of the primary slide are recorded in the range of 0.07–0.08 m/s.

By contrast, the flowslide failure does not show such a uniform deformation prior to the failure initiation. Instead, the local erosion gives rise to a stepwise movement pattern before the dominant flows arise from the crest of the slope. This movement pattern renders much larger peak velocities in the range of 0.2–0.5 (1.0) m/s prior at the initial failure state. According to the classification proposed by Cruden and Varnes [7], the velocities of most slopes following flowslide failure are classified as very rapid or to velocity class 6. This implies that it is difficult to operate evacuation if such rapid landslides occur [13].
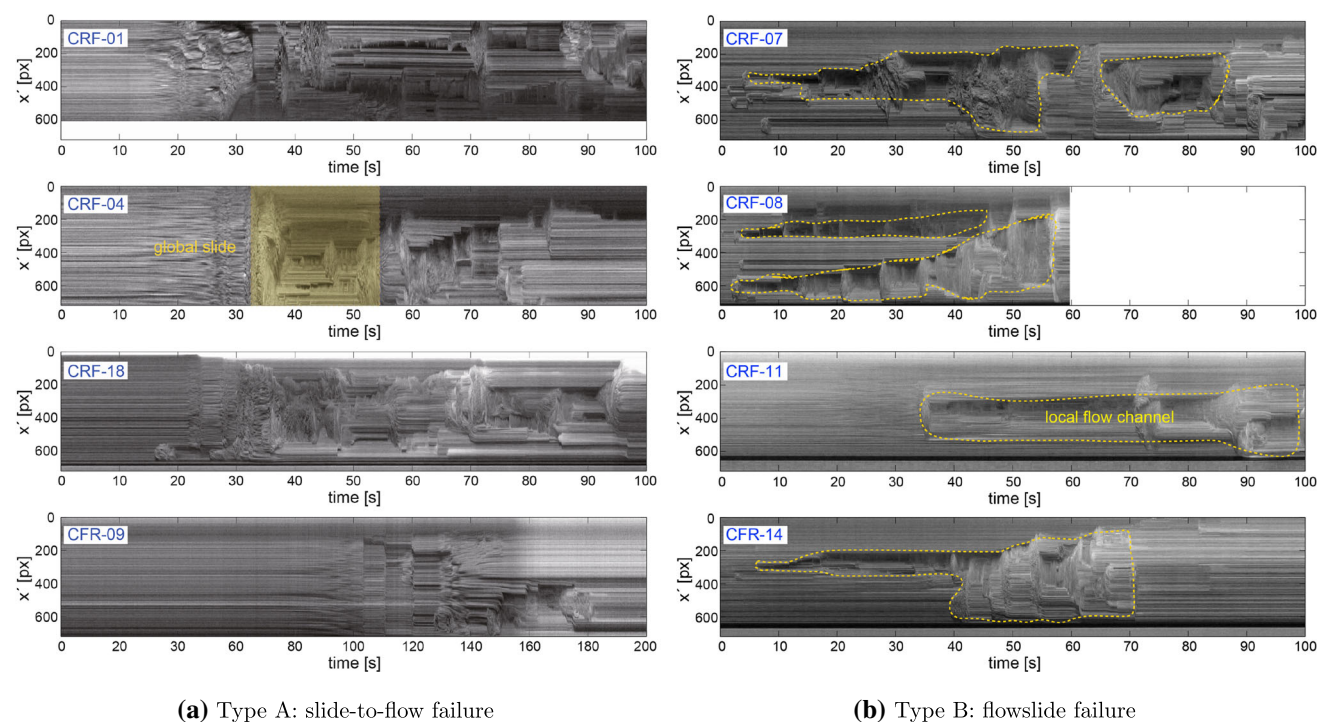

(a) Type A: slide-to-flow failure

(b) Type B: flowslide failure

Fig. 10 Surface space–time plots of rainfall-induced instability with different failure patterns: a slide-to-flow characterized by global slides and b flowslide characterized by local flow channels
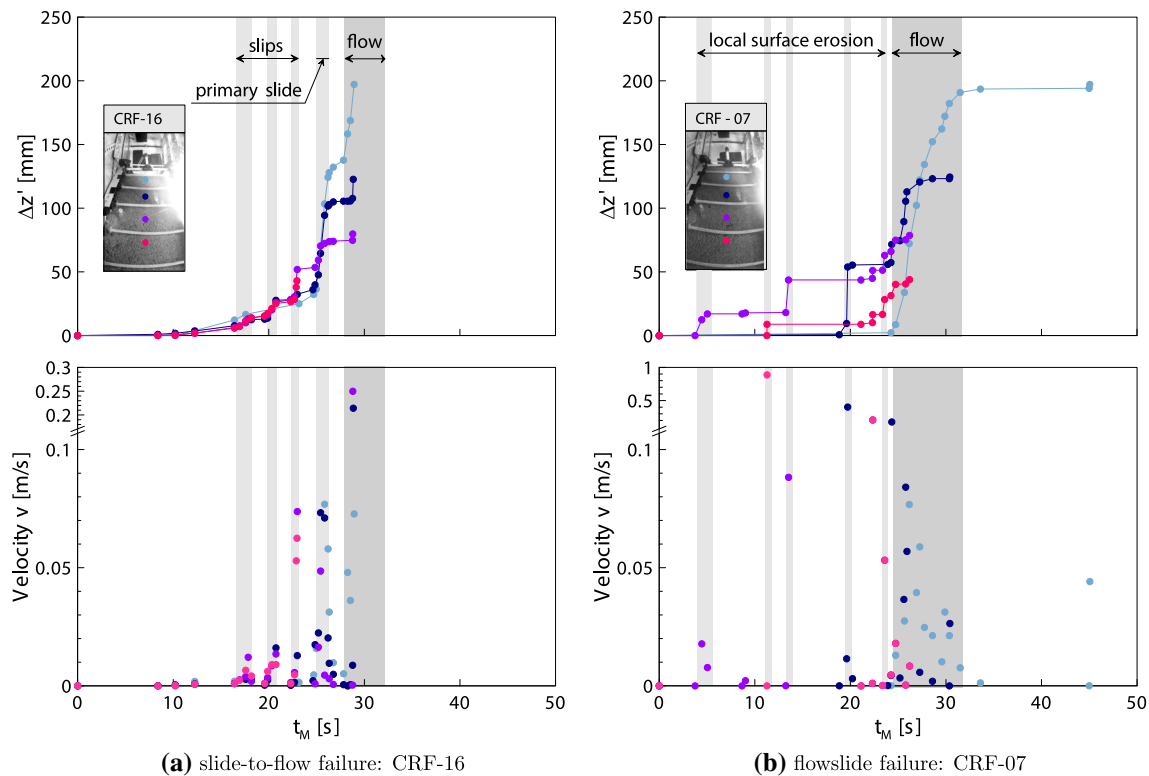
Fig. 11 Displacement paths and velocities of selected the soil at the surface of **a** slope CRF-16 following slide-to-flow failure and **b** slope CRF-07 following flowslide failure

4 Result analyses

The application of rainfall has successfully caused 16 out of the 18 slopes to failure with different types. In the following, the influences of rainfall intensities and initial slope conditions, e.g. slope angle, porosity and degree of saturation, on the failure initiations and failure types of the slopes are analysed.

4.1 Influence of rainfall intensity

The results of the rainfall applied to all the slopes and the initial failure time are depicted in Fig. 12. It can be seen that the slopes exposed in the moderate rainfall events with intensity about 5 mm/h are able to withstand much longer rainfall duration among all the slopes. The slope CRF-09, with medium dense compaction and 45° gradient, fails after 94 s or approximately 24 h at the prototype scale. The other slope CRF-10, only with a lower initial degree of saturation, does not experience any failure after a rainfall duration of 410 s or more than 4 days at the prototype scale.

The heavy rainfall of 12 mm/h is applied to 10 slopes inclined at 45° and 5 slopes inclined at 35°. Depending on the initial void ratio and initial degree of saturation, the rainfall durations causing initial failure range from 12 to 154 s (3 h to 1.5 days for the prototype) for 45° slopes and from 36 to 254 s (9 h to 2.7 days for the prototype) for 35° slopes. Of all the cases, the torrential rainfall of 27 mm/h on slope CRF-08 triggers the fastest failure. The rainfall duration is only approximately 4 s or approximately 1 h at the prototype scale. A comparison of all tests suggests that the rainstorm is more likely to trigger a flowslide, while a moderate rainfall event with long durations may give rise to slide-to-flow failure.

Figure 13 illustrates the failure surface and deposition of some slopes with similar initial conditions ($\beta_0 = 45°$, $e_0 \approx 0.74$ and $w_0 \approx 11.5\%$) but varying rainfall intensities from 4.9 to 27.0 mm/h. Clearly, the rainfall intensity has significant impacts on the slope failure, failure surface and final deposition. As shown in Fig. 13a, the moderate rainfall hardly causes the slope to failure, and only self-weight compaction is observed in the slope. With increasing the rainfall intensity to about 12.0 mm/h, the slopes first slide along a shear surface and then flow rapidly with continuous rainfall. As shown in Fig. 13b, c, subjected to heavy rainfall events, the slopes CRF-06 and CRF-18 exhibit a slide-to-flow failure pattern. It is observed that the slope CRF-08 (see Fig. 13d) fails immediately after a few seconds of torrential rainfall. A fast flowslide is initiated from the top of the slope with a high degree of saturation under such heavy rainfall. The short duration of torrential rainfall
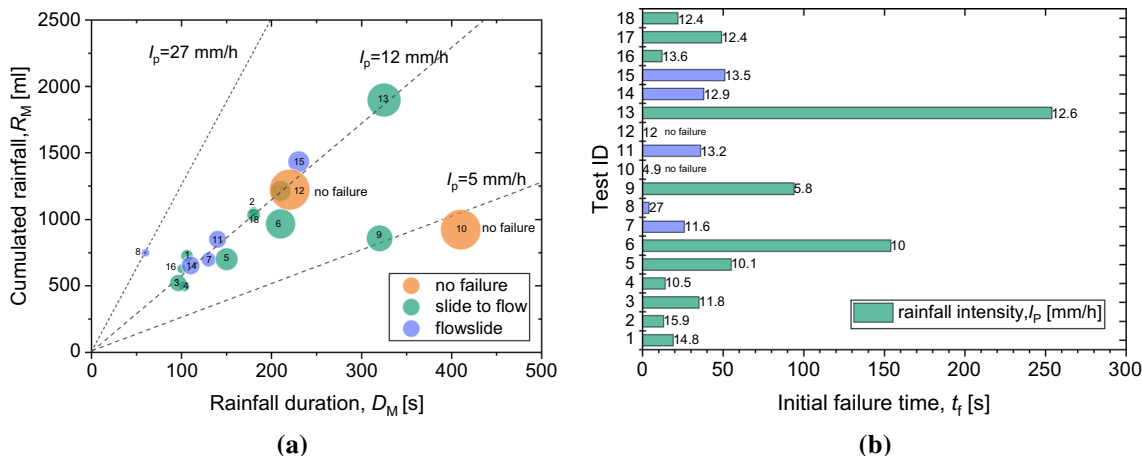
Fig. 12 Summary of the rainfall events: **a** the bubble graph of rainfall duration and cumulated rainfall (the size of the bubble denotes the initial failure time, and the number inside the bubble denotes the test ID). Note that slopes 10 and 12 did not fail; and **b** initial failure time of all slopes under variable rainfall intensity I_p

also causes the increase in the water level at the toe, where the soil is fully saturated with positive pore pressure.

A close inspection of the failure depositions suggests that the depth of a shear surface is related to the applied rainfall intensity. For slides turning into flows, a heavier rainfall event could lead to a deeper failure surface, mobilizing more sliding masses. Moreover, the torrential rainfall event is more likely to cause flowslides. However, it is believed that whether rainfall causes slope failure or not and the corresponding failure patterns are dependent not only on rainfall intensities but also on initial slope conditions.

4.2 Influence of initial slope condition

The initial conditions of slopes, represented by the slope angle, the void ratio of the slope soil and the profiles of the degree of saturation, are usually dependent on antecedent hydrologic and stress conditions. These conditions control the hydraulic conductivity, the quantity of water required to reach full saturation and the hydraulic gradient of the slopes. They play an important role in the saturation process and the development of positive pore pressures in the slopes [18]. Figure 14 shows the initial slope conditions on the failure initiations and failure types of the 16 failed slopes.
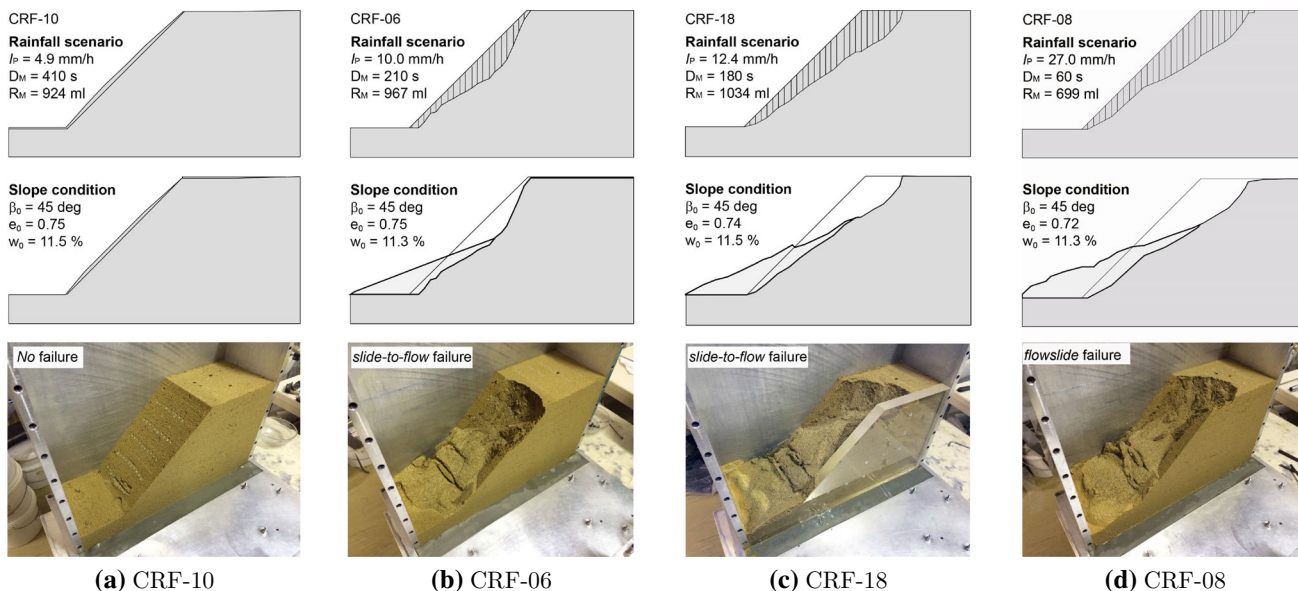

Fig. 13 Influence of rainfall intensity on the deposition and failure surface of the slopes with low initial void ratio and low water content
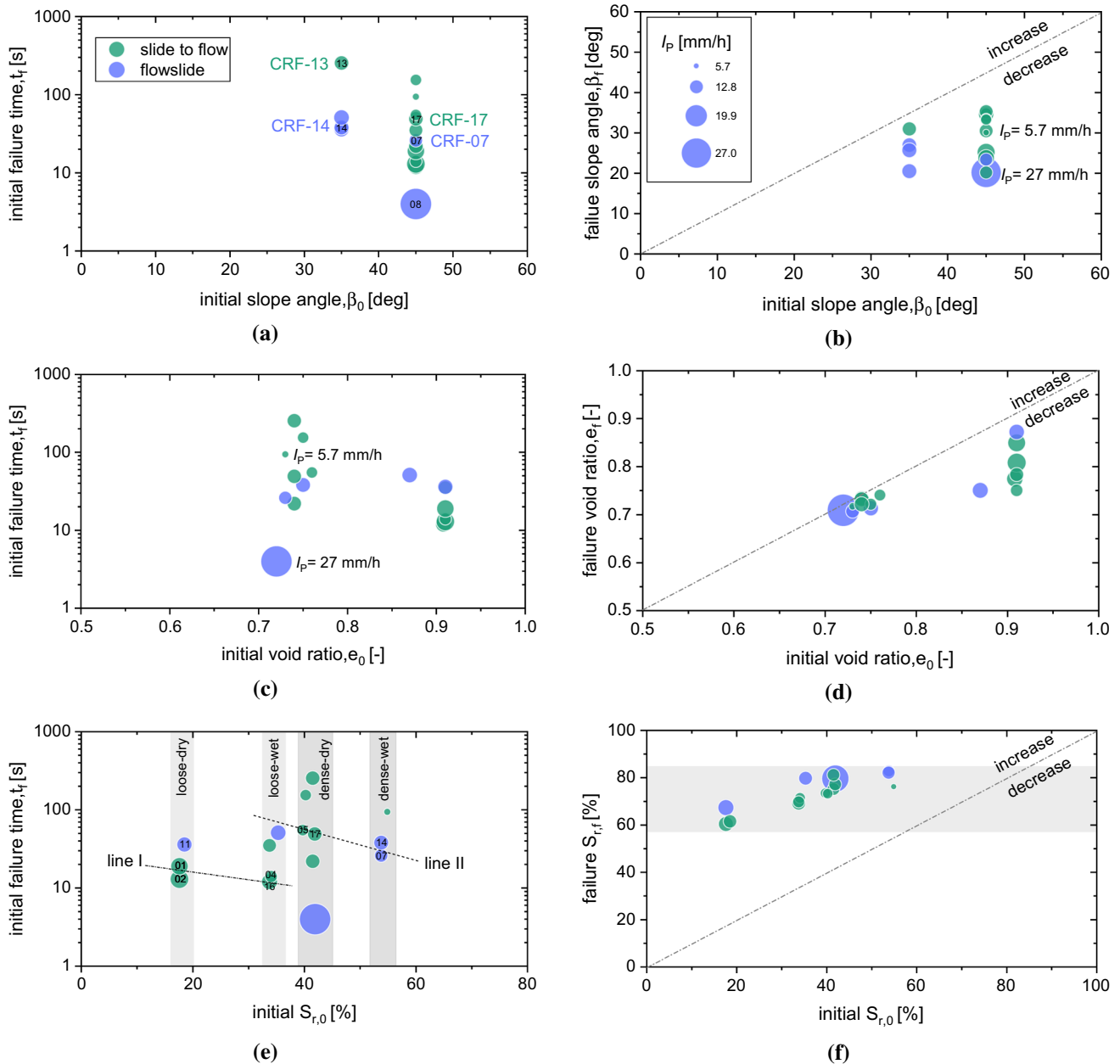
Fig. 14 Influences of initial slope angle, porosity and degree of saturation on the failure states and failure pattern of slopes. The size of the bubble denotes the rainfall intensity. Line I and II are defined by selected slopes with the similar e_0 but different $S_{r,0}$

Firstly, it can be anticipated that a slope with a steeper inclination is more prone to failure when exposed to rainfall. As shown in Fig. 14a, with the same initial conditions and rainfall intensities, the 35° slopes CRF-13 and CRF-14 are able to withstand longer rainfall duration compared to their counterparts CRF-17 and CRF-07, respectively. The critical rainfall duration for 35° slopes is about 2–4 times longer than those for the 45° slopes. After failure, the inclination angles of the deposited soil mass decrease to the range of 25°–35° (see Fig. 14b). The deposited soil masses of 45° slopes usually have longer distal reaches than those

of the 35° slopes, indicating the high mobility of the slope failures.

Secondly, it is known that an increase in the soil density leads to a significant decrease in the permeability but an increase in the shear strength of the soil (see Fig. 5). Therefore, a slope with denser initial compaction is able to sustain longer rainfall duration. As shown in Fig. 14c, the slopes compacted to a denser state, i.e. $e_0 \approx 0.74$, generally withstand up to 2 times longer rainfall durations. The soil density at failure condition can be obtained through back analysis considering the compaction during the test.

Figure 14d compares the void ratios at initial and failure states. It can be seen that the void ratios of slopes with medium dense compaction remain almost unchanged, while the slopes with loose density experience significant self-weight compaction prior to rainfall and wetting collapse within the wetting zone during rainfall. It is noticed that some of the initially loose soils even reach a medium dense state, especially slopes of that withstand longer rainfall durations.

Thirdly, the critical rainfall duration decreases with the initial degree of saturation or the antecedent rainfall. As shown by the lines I and II in Fig. 14e, the t_f decreases with $S_{0,r}$ for slopes with similar initial densities and rainfall intensities. It seems that the reduction gradient is relevant to the initial density of the slopes. Figure 14f plots the degree of saturation at both the initial and the failure states. It is observed that $S_{r,f}$ for all failed slopes increases significantly after rainfall. The degree of saturation at failure lies in the range of 0.6–0.8. It can be speculated that when the degree of saturation in the soil increases to this extent, the capillary forces become insufficient to maintain the slope stable, and thus, catastrophic failure of the slope may occur.

On the other hand, the failure surface and final deposition of the slopes are also related to the initial slope conditions. Figure 15 presents the origin and final deposition of some selected slopes with varying initial conditions but similar rainfall intensities. As shown in Fig. 15a, the slope CRF-13 is the only slope failed due to the local collapse at the toe under continuous rainfall infiltration. The rainfall duration causing the initial failure, $D_P \approx 60$ hours, is the longest among all tests. With a higher initial degree of saturation, however, the slope CRF-14 gives rise to flow-slides (see Fig. 15b) with a much larger sliding mass. On the other hand, it seems that the initial void ratio has less impact on the failure pattern and final deposition on the slopes. Figure 15c, d shows that, with a denser compaction state, the slope CRF-17 gives rise to a slightly deeper shear surface than that of the slope CRF-17. However, both slopes exhibit the slide-to-flow failure pattern under the heavy rainfall event. Furthermore, a comparison between the failure patterns and final depositions of 35° and 45° slopes implies that a gentler slope is more prone to flow-slides, while a steeper slope usually generates more sliding masses with deeper shear surfaces when failures occur.

According to Cascini et al [5], the main difference between slides turning into flows and flowslides lies on the difference in generation of pore water pressure at failure. Flowslides usually occur with either fully or partially undrained failure of soil mass in diffuse types, characterized by the generation of excess pore water pressure, along with strong hydromechanical coupling between fluid and solid phases. Thus, the eventual sudden acceleration of the failure mass is a consequence rather than a cause of the slope instability process [4, 5]. By contrast, drained failure of localized type may take place at the critical state when slides turning into flows. Previous studies [25, 30, 31] suggest that landslides in loose unsaturated soils with low hydraulic conductivity are prone to flowslide failure upon rainfall infiltration. Our experiments indicate that flowslide failure can occur in both dense and loose state. This phenomenon is also observed in other centrifuge tests on rainfall-induced slope failure [42]. The evidence we gain from the experiments suggests that the key factors,
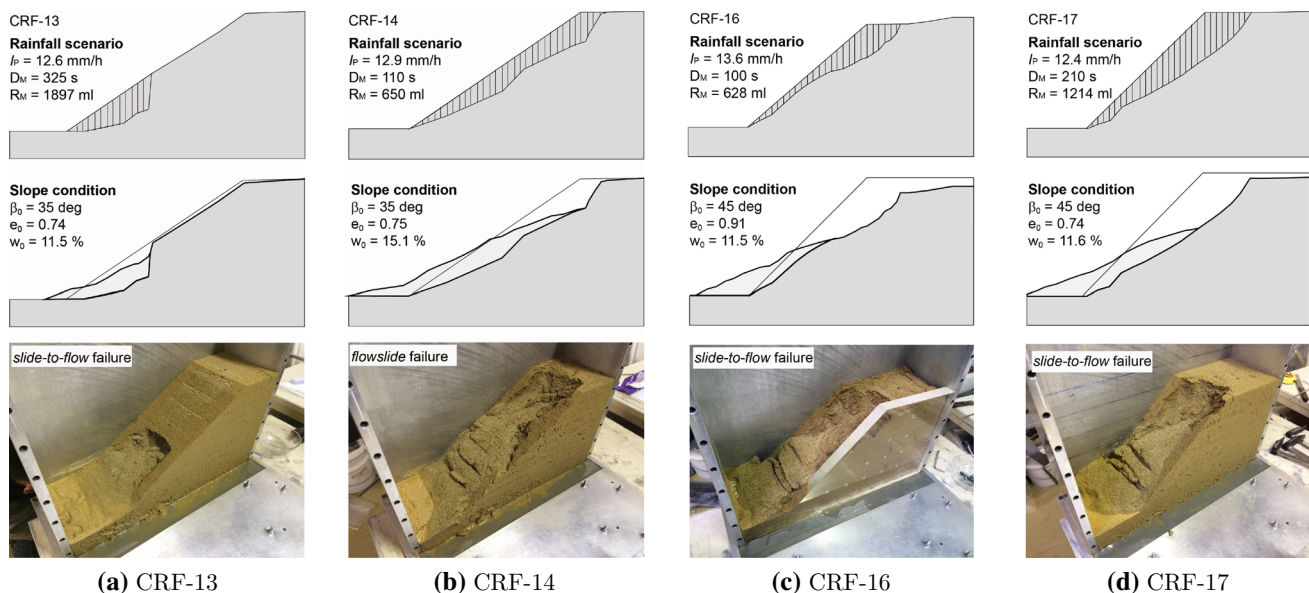

(a) CRF-13   **(b)** CRF-14   **(c)** CRF-16   **(d)** CRF-17

Fig. 15 Influence of soil initial condition on the failure surface and final deposition of selected slopes with different initial slope conditions

increasing the probability of flowslide failure, are fast saturation of soil at the vicinity of the slope due to high rainfall intensities, high antecedent rainfall events and low slope inclinations. All these factors facilitate the generation of excess pore water pressure upon rainfall infiltration. However, to quantify the roles of those factors in the development of flowslides or slides turning into flows, a quantitative measurement of the pore water pressure during precipitation is required.

5 Threshold curve

The relationship between rainfall events and the transient reduction of slope stability is significant for the prediction of landslide failure. The rainfall conditions that could trigger failure can be determined by empirical approaches. One of the most popular tools is the threshold curve, which determines the critical conditions of slope failure initiation. In the following, two threshold curves are introduced based on the experiments.

5.1 ID threshold curves

Firstly, the equation relating rainfall intensity (I) and duration (D), i.e. the ID threshold, defines the minimum rainfall duration for a given rainfall intensity at which slopes are likely to fail. The ID threshold was firstly proposed by Caine [3] to construct a global threshold for the occurrence of shallow landslides. Since then, the ID threshold is widely used at the local, regional and global scales [10, 11, 28, 37]. The ID threshold curve usually follows the following power function:

$$I = \alpha D^{-\beta} \tag{4}$$

where α and β are empirical parameters defined by means of statistical analyses.

In this work, a new ID threshold curve is proposed on the basis of the experiments. Figure 16a shows the proposed threshold curve in the log–log scale ($\alpha = 20.5, \beta = -0.77$). The threshold curve clearly shows that the slope failure is more likely to occur during torrential rainfall events with short duration or moderate rainfall events with long periods. Additionally, some threshold curves from the literature [3, 11, 28, 37] are selected for comparison. The proposed ID threshold curve fits between two published regional curves (5 and 6). A good agreement with the global threshold curves (curve 2a for low void ratio and 2b for high initial saturation) defined by Sidle and Ochiai [37] is also observed. A comparison between all the presented curves in Fig. 16a suggests that the global relationships seem to yield much lower thresholds than the regional one. Similar conclusion is also reported by Guzzetti et al. [10]. These ID threshold curves allow a simple definition of the rainfall necessary to provoke shallow instability on undisturbed slopes. Therefore, the estimated threshold may be applied to the quantitative evaluation of natural hazards associated with shallow landslides and debris flows [3]. But bearing in mind that, in addition to climate types, the threshold curves are subjected to the effects of many other factors, such as slope geometry, soil types and the hydraulic properties [22].
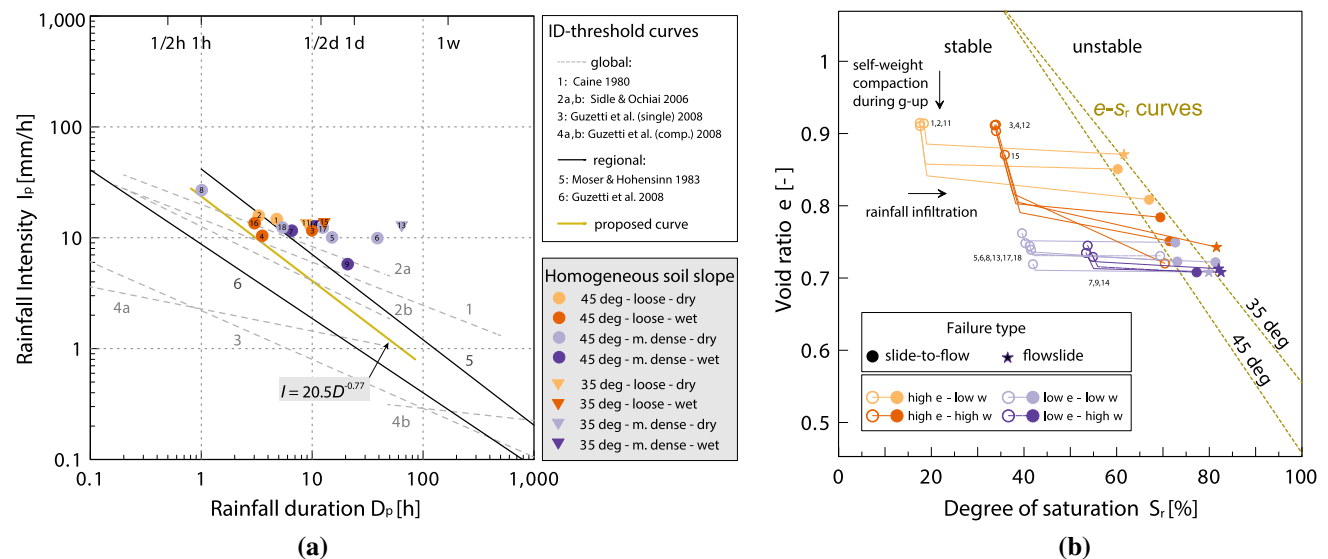

Fig. 16 Threshold curves **a** comparison the proposed ID threshold curve with those from the literature, **b** evolution of S_r and e during g-up compaction and rainfall of all tests

5.2 $S_r - e$ threshold curve

Despite widely used in some early-earning systems, the ID threshold curves could not reflect the influence of the initial slope conditions. To remedy this limitation, one may use the $S_r - e$ threshold curve to reflects the soil's reaction to the increase in the soil saturation in terms of the critical soil state. To this end, we measured the degree of saturation at the failure state from the failed soil mass and the changes in void ratio from the recorded digital images. Figure 16b presents the variation of the soil states, such as the initial condition, the condition after self-weight compaction during g-up and the failure condition, during the rainfall experiments. The final condition is indicated by different symbols to differ the failure mechanism.

The compaction and wetting paths of the slopes by means of the degree of saturation of the wetting zone versus its void ratio are also illustrated, assuming that the void ratio and degree of saturation vary linearly during the rainfall. This is reasonable since the degree of saturation increases with the rainfall during, as showing in Fig. 8. The dashed lines in Fig. 16b represent the $S_r - e$ threshold curves, defining the critical degree of satiation as a function of the void ratio. The $S_r - e$ functions for slopes with different inclinations as follows:

$$S_{r,f} = 1.69 - 1.24e \tag{5}$$

for 35° slopes and

$$S_{r,f} = 1.48 - 1.05e \tag{6}$$

for 45° slopes.

An inspection of the threshold curves suggests that the curve for 45° slopes is much steeper, indicating those slopes are more susceptible to the variation of saturation degree. This observation is confirmed by some numerical simulations of rainfall-induced slope instabilities [34]. The slopes with lower initial degree of saturations, e.g. slopes CRF-1, CRF-12 and CRF-11, tend to fail with lower final degree of saturation. It is also found that most of the slopes following the flowslide failure type yield higher degree of saturation than those of the slide-to-flow failure type, with the only exception of slope CRF-11, for which the slope surface has a higher degree of saturation (or water content) but lower internal friction (denoted by the blow number in the penetrometer test) than the other parts, as shown in Fig. 17. This result proves again the important role of the degree of saturation in the development of flowslides.
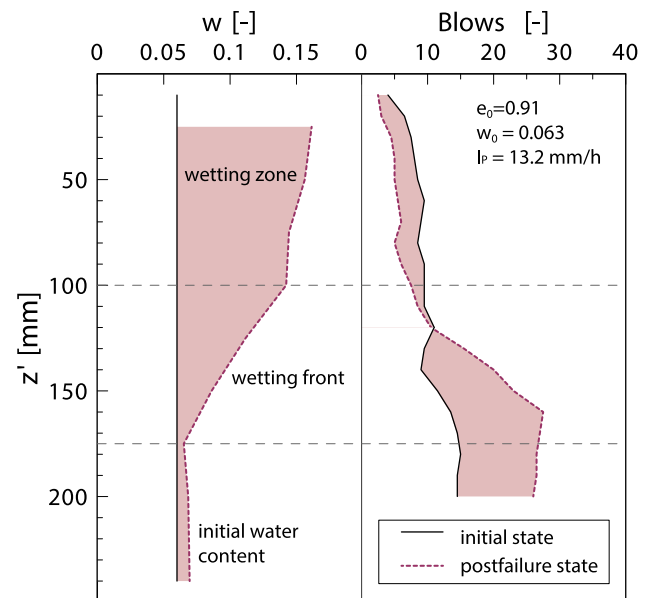

Fig. 17 Profiles of water content and penetrometer of slope CRF-11 at the initial and postfailure states (measured from the crest of the slope)

6 Conclusions

In this paper, we investigate the failure initiation and postfailure kinematics of rainfall-induced slope instabilities through centrifuge modelling. A group of small-scale model slopes with different initial conditions, e.g. slope geometry, porosity and degree of saturation, are exposed to rainfall of different intensities. The following conclusions can be drawn from the experiments:

Most of the slopes exhibit a flow-type failure pattern, either following the slide-to-flow or the flowslide failure modes. The slide-to-flow failure is initiated by a primary shallow slide, extending over the full height of the slope. With continuous precipitation, flow-type failure emerges from the unveiled and destabilized crest of the slope. The deformation analysis indicates a push-type failure mechanism with a shallow shear surface. On the other hand, the flowslide failure is initiated by the rapid increase in the pore water pressure at the slope surface, resulting in erosion channels and fast flowslides. The velocities of the flowslides are found to be in the range of 0.2–0.5 m/s, which is much larger than those of the slides turning into flows. The evidence we have suggests that fast saturation of soil at the vicinity of the slope, high antecedent rainfall events and low slope inclinations may increase the probability of flowslide failure.

An intensity–duration (ID) threshold curve is proposed to determine the critical rainfall duration that triggers slope failure. The new ID threshold curve fits closely to global thresholds. In addition, a $S_r - e$ threshold curve is introduced to decipher the relationship between porosity and

degree of saturation during rainfall infiltration. It is found that the critical saturation degree for flowslides is generally larger than that of the slides turning into flows, proving again the importance of the degree of saturation in the development of flowslides.

Data availability The datasets generated during and/or analysed during the current study are available from the corresponding author on reasonable request.

References

1. Alonso EE, Gens A, Josa A (1990) A constitutive model for partially saturated soils. Géotechnique 40(3):405–430
2. Cabrera MA, Wu W (2017) Experimental modelling of free-surface dry granular flows under a centrifugal acceleration field. Granular Matter 19(4):78
3. Caine N (1980) The rainfall intensity-duration control of shallow landslides and debris flows. Geografiska annaler 62(1–2):23–27
4. Cascini L, Cuomo S, Pastor M, Sacco C (2013) Modelling the post-failure stage of rainfall-induced landslides of the flow type. Can Geotech J 50(9):924–934
5. Cascini L, Cuomo S, Pastor M, Sacco C (2013) Modeling of rainfall-induced shallow landslides of the flow-type. J Geotech Geoenviron Eng 136(1):85–98
6. Collins BD, Znidarcic D (2004) Stability analyses of rainfall induced landslides. J Geotech Geoenviron Eng 130(4):362–372
7. Cruden DM, Varnes DJ (1996) Landslide types and processes. Transportation research board special report vol 247, pp 36–75
8. Darve F, Laouafa F (1996) Instabilities in granular materials and application to landslides. Mech Cohes. Frict. Mater 5(8):627–652
9. Darve F, Laouafa F (1996) Equations for the soil-water characteristic curve. Can Geotech J 31(4):521–532
10. Guzzetti F, Peruccacci S, Rossi M, Stark CP (2007) Rainfall thresholds for the initiation of landslides in central and southern Europe. Meteorol Atmos Phys 98:239–267
11. Guzzetti F, Peruccacci S, Rossi M, Stark CP (2008) The rainfall intensity-duration control of shallow landslides and debris flows: an update. Landslides 5(1):3–17
12. Hungr O (2004) Flow slides and flows in granular soils. In: Proceedings of international workshop flows 2003—occurrence and mechanisms of flows in natural slopes and earthfill. L. Picarelli, ed., Patron, Bologna
13. Hungr O, Leroueil S, Picarelli L (2014) The Varnes classification of landslide types, an update. Landslides 11(2):167–194
14. Idinger G, Wu W (2019) Failure of unsaturated soil slopes initiated by self-weight loading. Recent Adv Geotech Res, pp 91–103
15. Johnson KA, Sitar N (1990) Hydrologic conditions leading to debris-flow initiation. Can Geotech J 27(6):789–801
16. Kimura K (1991) Failure of fills due to rain fall. In Centrifuge, 91, pp 509–516. Balkema
17. Lee K, Suk J, Kim H, Jong S (2020) Modeling of rainfall-induced landslides using a full-scale flume test. Landslides. https://doi.org/10.1007/s10346-020-01563-8
18. Leroueil S (2001) Natural slopes and cuts: movement and failure mechanisms. Géotechnique 51(3):197–243
19. Leroueil S (2004) Geotechnics of slopes before failure. In: Stabilization WA, Lacerda M, Ehrlich SAB, Fontoura, Sayao ASFJ (eds) Landslides: evaluation and Vol. 1, Taylor and Francis, London, pp 863–884
20. Lim TT, Rahardjo H, Chang MF, Fredlund DG (1996) Effect of rainfall on matric suctions in a residual soil slope. Can Geotech J 33:618–628
21. Ling H, Ling HI (2012) Centrifuge model simulations of rainfall-induced slope instability. J Geotech Geoenviron Eng 138(9):1151–1157
22. Ling HI, Wu MH, Leshchinsky D, Leshchinsky B (2009) Centrifuge modeling of slope instability. J Geotech Geoenviron Eng 135(6):758–767
23. Liu QB, Lehane BM (2012) The influence of particle shape on the (centrifuge) cone penetration test (CPT) end resistance in uniformly graded granular soils. Géotechnique 62(11):973–984
24. Lizárraga JJ, Buscarnera G (2018) Safety factors to detect flowslides and slips in unsaturated shallow slopes. Géotechnique 68(5):442–450
25. Lourenco S, Sassa K, Fukuoka H (2006) Failure process and hydrologic response of a two layer physical model: Implications for rainfall-induced landslides. Geomorphology 73(1–2):115–130
26. Lu N, Godt JW (2013) Hillslope hydrology and stability. Cambridge University Press vol 73, pp 115–130
27. Moriwaki H, Inokuchi T, Hattanji T, Sassa K, Ochiai H, Wang G (2004) Failure processes in a full-scale landslide experiment using a rainfall simulator. Landslides 1(4):277–288
28. Moser M, Hohensinn F (2016) Geotechnical aspects of soil slips in Alpine regions. Eng Geol 19(3):185–211
29. Mualem Y (1976) A new model for predicting the hydraulic conductivity of unsaturated porous media. Water Resour Res 12(3):513–522
30. Olivares L, Picarelli L (2003) Shallow flowslides triggered by intense rainfalls on natural slopes covered by loose unsaturated pyroclastic soils. Géotechnique 53(2):283–287
31. Picarelli L, Olivares L, Damiano E, Darban R, Santo A (2020) The effects of extreme precipitations on landslide hazard in the pyroclastic deposits of Campania Region: a review. Landslide 17:2343–2358
32. Pirone M, Papa R, Nicotera MV, Urciuoli G (2015) situ monitoring of the groundwater field in an unsaturated pyroclastic slope for slope stability evaluation. Landslides 12(2):259–276
33. Rahardjo H, Li XW, Toll DG, Leong EC (2001) The effect of antecedent rainfall on slope stability. Geotech Geol Eng 19(3–4):371–399
34. Rahardjo H, Ong TH, Rezaur RB, Leong EC (2007) Factors controlling instability of homogeneous soil slopes under rainfall. J Geotech Geoenviron Eng 133(12):1532–1543

35. Rahardjo H, Ong TH, Rezaur RB, Leong EC, Fredlund DG (2010) Response parameters for characterization of infiltration. Environ Earth Sci 60:1369–1380

36. Rouainia M, Helm P, Davies O, Glendinning S (2020) Deterioration of an infrastructure cutting subjected to climate change. Acta Geotech 15:2997–3016

37. Sidle R, Ochiai H (2006) Landslides: processes, prediction, and land use. Water resources monograph, American Geophysical Union, Washington

38. Song YS, Chae BG, Lee J (2016) A method for evaluating the stability of an unsaturated slope in natural terrain during rainfall. Eng Geol 210:84–92

39. Sorbino G, Nicotera MV (2013) Unsaturated soil mechanics in rainfall-induced flow landslides. Eng Geol 165:105–132

40. Springman SM, Jommi C, Teysseire P (2003) Instabilities on moraine slopes induced by loss of suction: a case history. Géotechnique 53(1):3–10

41. Take WA, Beddoe RA (2014) Base liquefaction: a mechanism for shear-induced failure of loose granular slopes. Can Geotech J 51(5):496–507

42. Take WA, Bolton MD, Wong PCP, Yeun FJ (2004) Evaluation of landslide triggering mechanisms in model fill slopes. Landslides 1(3):173–184

43. Take WA, Beddoe RA, Davoodi-Bilesavar R, Phillips R (2015) Effect of antecedent groundwater conditions on the triggering of static liquefaction landslides. Landslides 12(3):469–479

44. Taylor RN (2018) Centrifuges in modelling: principles and scale effects. In Geotechnical Centrifuge Technology, pp 19–33. CRC Press

45. Vandenboer K, Celette F, Bezuijen A (2019) The effect of sudden critical and supercritical hydraulic loads on backward erosion piping: small-scale experiments. Acta Geotech 14:783–794

46. Wang R, Zhang G, Zhang JM (2010) Centrifuge modelling of clay slope with montmorillonite weak layer under rainfall conditions. Appl Clay Sci 50(3):386–394

47. Wang S, Idinger G (2020) A device for rainfall simulation in geotechnical centrifuges. Acta Geotechnica. https://doi.org/10.1007/s11440-021-01186-w

48. White DJ, Take WA, Bolton MD (2003) Soil deformation measurement using particle image velocimetry (PIV) and photogrammetry. Géotechnique 53(7):619–631

49. Zhang G, Qian JY, Wang R, Zhang JM (2011) Centrifuge model test study of rainfall-induced deformation of cohesive soil slopes. Soils Found 51(2):297–305